PERGAMON

International Journal of Solids and Structures 38 (2001) 4119–4145

INTERNATIONAL JOURNAL OF SOLIDS and STRUCTURES

www.elsevier.com/locate/ijsolstr

Influence of nonlinearity and double elasticity on flexure of rock beams — II. Characterization of Dionysos marble

G.E. Exadaktylos [a,*], I. Vardoulakis [b], S.K. Kourkoulis [b]

[a] *Rock Mechanics Laboratory, Department of Mineral Resources Engineering, Technical University of Crete, GR-73100 Chania, Greece*
[b] *Department of Engineering Science, Section of Mechanics, National Technical University of Athens, 5, Heroes of Polytechnion Avenue, Zografou Campus, GR-15773 Athens, Greece*

Received 28 January 1999

Abstract

A technical bending theory of beams accounting for nonlinearity due to damage and bimodularity of brittle rocks was proposed in Part I. In order to check the validity of the above theory, a series of three-point bending (3PB) tests has been carried out using Dionysos marble beams that have been sampled from the same extracted block. Although the modeling of the 3PB test is considerably more complicated than that of the four-point bending test, the experimental procedure in the former test is simpler than in the later test and most importantly, the location of the fracture is better controlled in the 3PB test. Herein, it is demonstrated that the test results have very good repeatability and they support the above technical theory. The bending tests also indicate that Dionysos marble is characterized by different elastic modulus in compression (E_c) and in tension (E_t) at small loads, such that the relation $m = E_c/E_t \cong 0.8$ holds true. This relationship of elastic moduli for this type of marble is also supported independently by uniaxial compression and direct tension tests on test specimens cored from the same marble block. A plausible physical explanation for this type of marble anisotropy has yet to be made. This observed difference cannot be explained by considering the rock simply as a material with cracks. It may be attributed to pure micromechanical reasons such as the complex microstructure of this type of rock, characterized by a complex previous loading history (metamorphism). Until such an explanation is available, the apparent behavior can be used in analyzing the stress–strain behavior of rocks. Further, the 3PB experiments indicate that fracture of marble starts always at the bottom fiber of the middle cross-section of the beam and the failure extension strain is the same with that occurring in the direct tension test. This last result is due to the fact that the central section of marble beam is almost under extensional strain, which in turn is caused by the combination of the concentrated load and Poisson's effects. The damage parameter that enters the direct tension stress–strain law was obtained independently from longitudinal strain measurements at the outermost compression and extension fibers, as well as, from bending curvature and deflection measurements. This value of the damage factor is in accordance with the damage measured from the direct tension tests. It is also demonstrated that a linear Timoshenko-type theory containing an intrinsic length scale is able to approximate the nonlinear deflection behavior of Dionysos marble beams. Finally, based on a suggestion by Ludwig Prandtl, the stress–strain relationships in unconfined compression and direct tension, as well as Poisson's ratio, of Dionysos marble were derived from bending tests.

* Corresponding author. Address: 8, Lamias Str. GR-11523 Ambelokipi, Athens, Greece. Fax: +30-1-699-4116.
E-mail address: exadakty@mred.tuc.gr (G.E. Exadaktylos).

0020-7683/01/$ - see front matter
PII: S0020-7683(00)00252-3

Keywords: Nonlinearity; Elasticity; Rock beams; Dionysos marble

1. Introduction

The present experimental work constitutes a part of a research project devoted to the standardization and harmonization of rock mechanics element and structural tests employed for the characterization of natural building stones in historical monuments. These tests include the direct tension, unconfined and triaxial compression, bending of intact and pre-notched beams, ultrasonic, and surface instability tests. It will be applied to improve the restoration strategy of monuments made from natural building stones. The Parthenon Temple on the Acropolis of Athens, Greece is a specific site where the laboratory and in situ testing methodologies will be validated. It is obvious that the results of this study may also aid in the design and stability analysis of engineering structures in competent rock.

The repair work, in progress today, on the Parthenon temple of the Acropolis of Athens is the most extensive ever performed on the monument, which dates to the mid-fifth century BC (Korres, 1993). For this purpose, it is requisite to obtain an exact and in depth knowledge of the mechanical properties and strength of the materials used for the construction of the monument and those used for its restoration. The stone that is used almost exclusively for the restoration of Parthenon is Dionysos marble, which is a pure metamorphic calcitic rock, since it has the nearest physical and mechanical properties with the Pentelikon marble that was originally used by ancient Athenians for the construction of the monument.

An experimental program on the mechanical characteristics of marble used in restoration of Parthenon should begin with the time-honored direct tension test since (a) rocks are much weaker in tension, (b) axial cleavage fracturing of rocks in uniaxial compression obeys the maximum extension strain criterion (Stacey, 1981) with the critical extension strain to be a property directly measured from a uniaxial tension test, and (c) it is possible to use stress–strain and failure load or strain measurements, together with modern theories of strength and elasticity in order to predict the behavior of rocks under states of static combined stresses which occur so often in practice. A series of direct tension tests with specially designed tensile grips on dog-bone Dionysos marble specimens has been carried out by Vardoulakis et al. (1995, 1998) to determine the tensile stress–strain curve of the marble and to assess the repeatability of test results.

On the other hand, flexure testing of Dionysos marble is also indispensable in such an investigation for the following reasons: (i) to estimate the mechanical behavior of the marble in a nonuniform stress–strain state such as that produced during bending, (ii) to either indirectly assess the tensile strength of rocks due to the difficulty of performing direct tension tests or to investigate the comparability of bending test results with those derived from uniaxial element tests, such as the direct tension and unconfined compression tests, and (iii) structural members of marble in situ such as beams, architraves and corner architraves are subjected to bending loads.

In order to check the validity of the technical beam theory presented in Part I of this study (Exadaktylos et al., 2000), a series of three-point bending (3PB) tests has been designed and carried out using Dionysos marble beams. Although the modeling of the 3PB test is considerably more complicated – due to the ''punch effect'' and the variation of bending moment along the length of the beam – than that of the four-point bending (4PB) test, the experimental procedure in the former test is simpler than that in the later test and most importantly the location of the fracture is better controlled in the 3PB test. Thereafter, all the notations of physical and geometrical quantities are the same as those employed in Part I of this work.

2. Marble specimens and experimental procedure

2.1. Marble composition and tension–compression behavior

Dionysos marble consists of an equidimensional mosaic of fine calcite grains with straight to gently curved boundaries having an average size of 400 μm. Its mineralogical composition by weight is calcite 98%, quartz 0.5%, muscovite 0.5%, sericite 0.5%, chlorite 0.5%; however, some small percentage of dolomite may also be present in its composition. It has a unit weight of 26.7 $\mathrm{kN\,m^{-3}}$, porosity 0.371%, and absorption coefficient by weight 0.11%. The microscopic petrographical image with parallel Nicols of Dionysos marble is illustrated in Fig. 1.

Concerning the tensile properties of this type of marble, data showing rather considerable scattering have been reported in the literature (Zambas, 1994), and it is only recently that the authors obtained reliable and repeatable data concerning its constitutive stress–strain law (Vardoulakis et al., 1995, 1998). The main reasons for this scattering are the different conditions under which the experiments were executed, misalignment problems, and the anisotropic behavior of Dionysos marble.

A series of direct tension tests on Dionysos marble was performed by employing a special experimental setup that includes (a) special grips for dog-bone specimens, (b) a system of multi-point strain measurement in two directions with the aid of electric resistance strain gages feeding data directly to a PC, and (c) the suitable software for the evaluation and elaboration of the experimental data to obtain the true stress values. The following best fitted parabolic relation has been found to describe best the experimental data regarding the direct tension test for specimens loaded along the rift plane:

$$\begin{aligned} &\sigma_t = 85,000\varepsilon_t(1 - 1880\varepsilon_t), \quad 0 \leqslant \varepsilon_t \leqslant \varepsilon_{tu}, \\ &\sigma_{tu} = 11\ \mathrm{MPa}, \qquad \varepsilon_{tu} = 225 \times 10^{-6}, \end{aligned} \tag{1}$$

where σ_t is expressed in MPa and σ_{tu}, ε_{tu} represent the tensile stress and strain, respectively, at failure.

In Fig. 2(a), the axial stress–axial strain curve of the direct tension for Dionysos marble is illustrated. The correction of the primary data in order to eliminate eccentricities due to parasitic bending stresses was performed by properly processing the four axial strain measurements from the anti-diametrically attached strain gages at mid-height of the dog-bone specimens. According to a linear damage evolution law, the

Fig. 1. Typical optical micrograph of Dionysos marble.

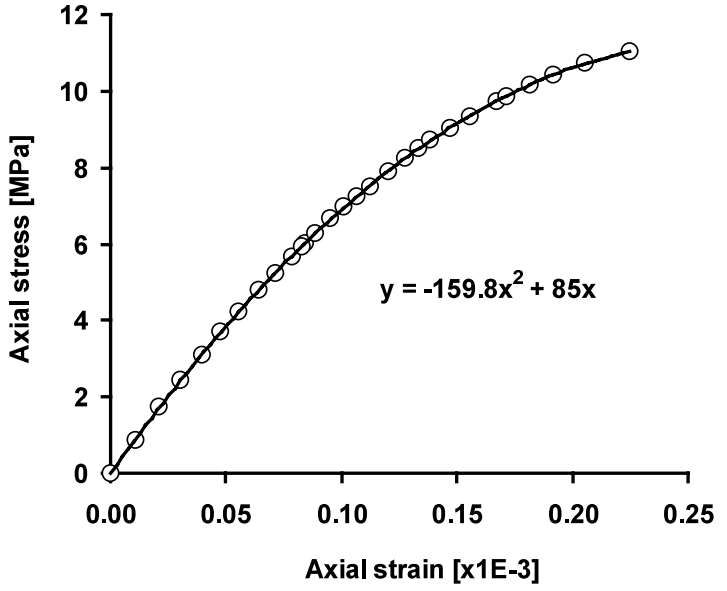

(a)

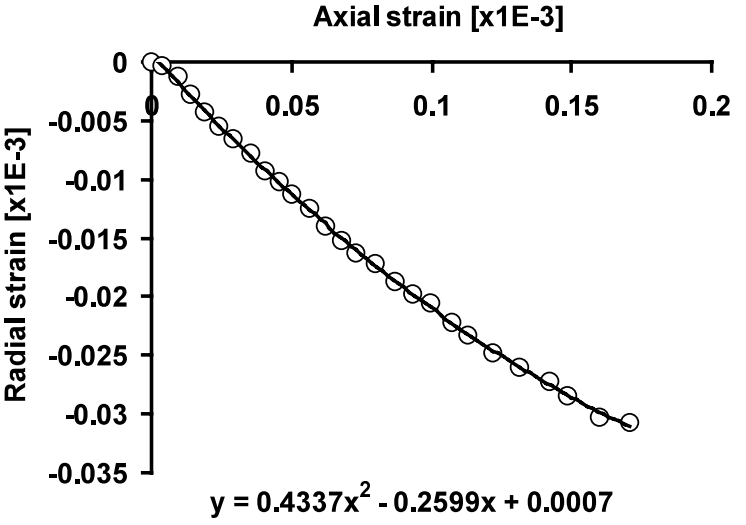

(b)

Fig. 2. (a) Plot of axial stress versus axial strain in uniaxial tension test of Dionysos marble. The dots represent values of the test, whereas the continuous line is after the appropriate correction procedure that eliminates bending strains during loading and (b) radial strain versus axial strain in uniaxial tension test of Dionysos marble.

experimental data indicate a smaller ultimate value of the damage factor with respect to that predicted by Gerstner's $d\sigma/d\varepsilon$ instability criterion

$$D_f = -m_f \varepsilon_{tu} = 1880 \times 225 \times 10^{-6} = 0.43. \tag{2}$$

Thus, the experimental data indicate that failure of the dog-bone specimen occurs when the effective area of the cross-section is reduced to 57% of the original intact area. The initial tangent Poisson's ratio of Dionysos marble may also be found to be $v_t = 0.26$ (Fig. 2(b)).

Further, a typical axial stress versus axial strain curve of Dionysos marble in uniaxial compression parallel to the rift plane of the marble for a height to diameter ratio equal to 2:1 and with lubricated specimen ends is illustrated in Fig. 3(a).

The best fitted cubic empirical law in the full range of experimental stress–strain points shown in Fig. 3(a) has the form

$$\begin{aligned} &\sigma_c = 73,679\varepsilon_c\left(1 + 464\varepsilon_c - 426,214\varepsilon_c^2\right), \quad 0 \leqslant \varepsilon_c \leqslant \varepsilon_{cu}, \\ &\sigma_{cu} = 85.2 \text{ MPa}, \qquad \varepsilon_{cu} = 1.4 \times 10^{-3} \end{aligned} \tag{3}$$

with σ_c expressed in MPa, and σ_{cu}, ε_{cu} represent the unconfined compression stress and strain, respectively, at failure. Further, the initial Poisson ratio was found from the best-fit linear curve of transverse strain versus axial strain at small loads (Fig. 3(b)) to be $v_c = 0.32$, which is larger than that obtained from the direct tension tests. Therefore, for Dionysos marble, the following experimental relation is valid

$$\frac{\sigma_{cu}}{\sigma_{tu}} = 7.74, \tag{4}$$

which is in reasonable agreement with the prediction of Griffith's brittle fracture theory (Griffith, 1924) that gives a strength ratio value of 8.

The above best fitted cubic law (3) is valid for the whole pre-peak stress regime, whereas in the case of bending, only the initial small deformation portion of the compression curve is effective. According to this rationale, the uniaxial compression data corresponding to the initial deformation range were fitted by a simpler approximate linear law in the small deformation range as follows (Fig. 4):

$$\sigma_c = 71,891\varepsilon_c, \quad 0 \leqslant \varepsilon_c \leqslant 1.5 \times 10^{-3}. \tag{5}$$

From Fig. 4, it may be seen that the parabolic law is fairly accurate in the considered strain regime for this type of rock due to its small porosity. Finally, the $\sigma_t = f(\varepsilon_t)$ curve in uniaxial tension and $\sigma_c = f(\varepsilon_c)$ in unconfined compression (by taking compressive stresses and strains negative) of Dionysos marble are illustrated in Fig. 5. A plausible physical explanation for this observed anisotropy in certain rock types has yet to be made. This observed difference – that may be realized as a special type of anisotropy – is possibly due to the complex microstructure and previous loading history of this type of metamorphic rock.

The combined σ–ε constitutive law in uniaxial tension–compression regimes may be described by the following relations:

$$\begin{aligned} &\sigma_t = 85,000\varepsilon_t(1 - 1880\varepsilon_t), \quad 0 \leqslant \varepsilon_t \leqslant 225 \times 10^{-6}, \\ &\sigma_c = 71,891\varepsilon_c, \quad -150 \times 10^{-6} \leqslant \varepsilon_c \leqslant 0, \\ &m_f = -1880, \qquad m_b = 0, \\ &\frac{E_c}{E_t} = 0.846. \end{aligned} \tag{6}$$

In the sequel, the behavior of Dionysos marble in 3PB is investigated, by employing the proposed technical theory developed in Part I, with the aim to derive the σ–ε constitutive law in uniaxial tension–compression regimes independently from appropriately designed bending tests.

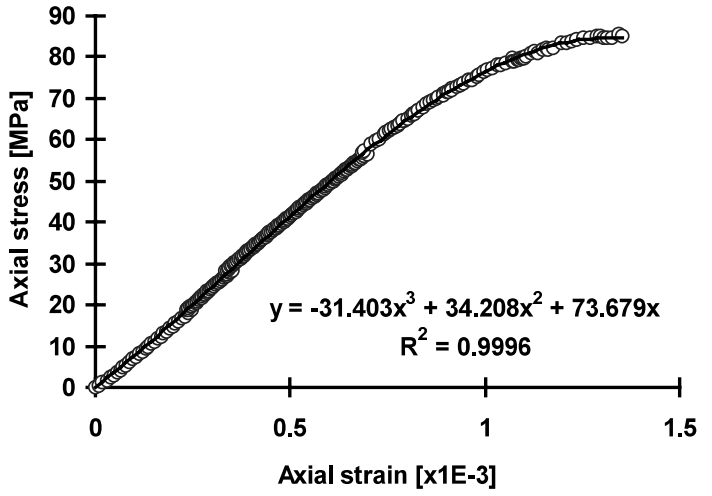

(a)

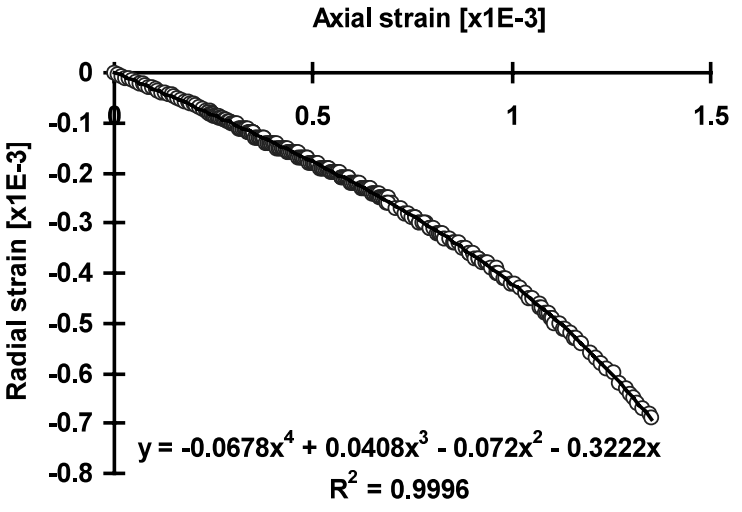

(b)

Fig. 3. (a) Plot of axial stress versus axial strain, and (b) transverse strain versus axial strain at small loads, in uniaxial compression test of Dionysos marble.

2.2. Bending experiments

A series of 3PB tests was executed with prismatic marble beams with their longer dimension parallel to the rift plane of the marble of length equal to 0.40 m and square cross-sections of dimensions 0.10×0.10 m^2. This series of tests was designed in such a manner so that to check (a) the validity of the proposed technical theory presented in Part I, (b) the repeatability of test results, (c) the symmetry of loading, (d)

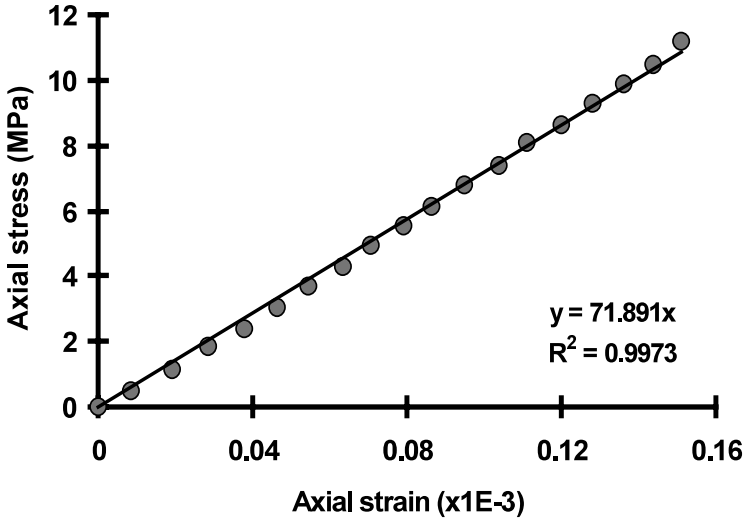

Fig. 4. Best fitted linear law in the small deformation regime of the uniaxial compression test data displayed in Fig. 3.

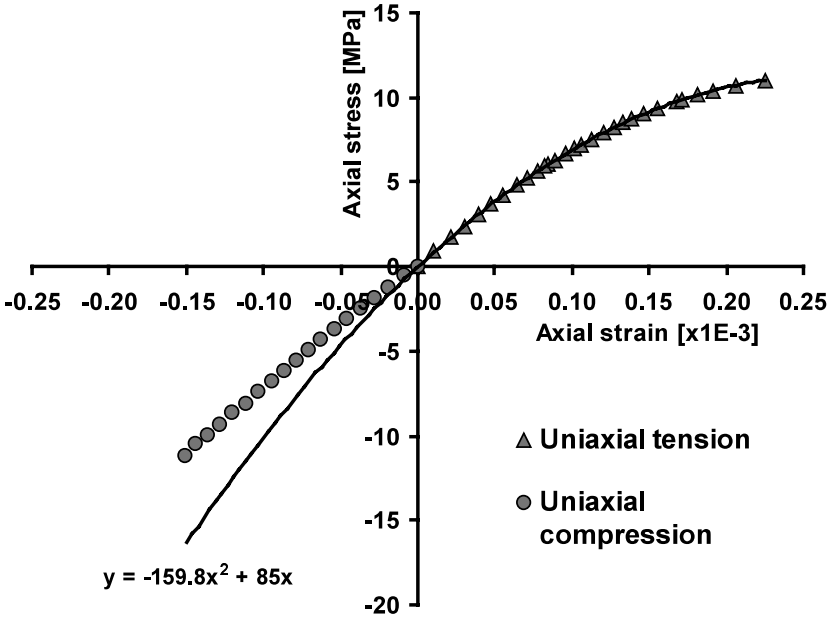

Fig. 5. Plot of axial stress versus axial strain in uniaxial tensile and compression regimes of Dionysos marble.

the mode of fracture, and (e) the behavior of marble beams in cyclic loading. The load was applied with the aid of a stiff 1000 kN Amsler hydraulic testing machine. The specimens were placed on two rollers of diameter 0.07 m and the load was applied uniformly along the thickness of the specimens with the aid of a third roller, as it is shown in the sketch of Fig. 1(a) in Part I. The loading direction was set perpendicular to the rift plane of the marble specimens that have been extracted from the same marble block from which

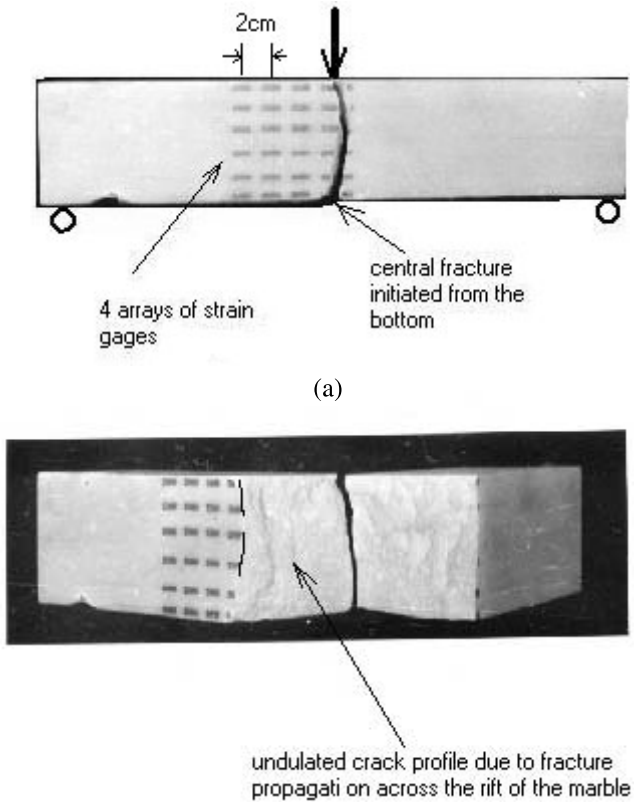

Fig. 6. (a) Dionysos marble specimen instrumented by strain gauges and (b) typical picture of a fractured specimen in 3PB.

the uniaxial tension and compression specimens were cored. For the measurement of the longitudinal strains ε_{xx}, 28 electric resistance strain gauges (Kyowa, KFG type) were employed, appropriately attached on four vertical sections of the beams, as is displayed in the photo of Fig. 6(a). In order to check the symmetry of experimental results about the middle section of the specimen, some experiments were conducted on specimens with an additional number of strain gauges attached at normal beam sections symmetrical to its middle section. Also, in some tests, the deflections were measured using four dial gauges placed in direct contact with the lower face of the specimens exactly at those normal sections on which strain gauges were attached. The load was applied monotonically with the rate of the motion of the grips not exceeding the value of 10^{-3} mm min^{-1}. The machine stiffness can be considered infinite compared to that of the marble specimens since the maximum load sustained by the latter was always lower than 35 kN.

As may be seen from the photograph of Fig. 6(b), the marble under 3PB fails by a single fracture at the central section which initiates always from the outermost lower fiber and propagates in an unstable manner in a direction more or less normal to the long axis of the specimen and towards the loading point. Crack surfaces although not perfectly plane are smooth, however, if observed closely, exhibit an undulated profile of very small amplitude.

Table 1
Failure load and maximum extension strain at the outermost fiber in the 3PB tests

3PB test no.	Failure load, P_F (kN)	Extension strain at failure load, ε_{tb} (μstrains)
I	27.5	235
II	31.5	214
III	34.5	231
IV	33.2	259
Mean	31.7	235
Standard deviation	3.0	18.6

3. Results of experiments and comparison with the theory

3.1. Strain distribution and punch effect

As is indicated in Table 1 where the results of some characteristic tests are shown, the failure load P_F, of Dionysos marble beams in 3PB varied between narrow limits, whereas the same holds also true for the outer-fiber extension strain measured at failure load. For all experiments executed, it holds true that the mean value and the standard deviation (s.d.) of the failure load were 31.7 and 3 kN, respectively. Also, the mean value and standard deviation of the maximum extension strain are equal to 235 and 18.6 μstrains, respectively.

The data displayed in Table 1 clearly demonstrate the acceptable repeatability of the executed 3PB tests on Dionysos marble with the relative standard deviation (coefficient of variation) of the failure load and maximum extension strain to be equal to 9.5% and 7.9%, respectively. Furthermore, an important relation between the failure tensile strain in 3PB and in direct tension for Dionysos marble that can be inferred from the comparison of Table 1 and the data presented in Section 2, respectively, is the following:

$$\frac{\varepsilon_{bu}}{\varepsilon_{tu}} \approx 1. \tag{7}$$

Based on the theoretical results presented in Part I, it may be remarked here that the $(d\sigma/d\varepsilon_t)$ failure criterion under simple tension loading predicts the ultimate extension strain in 3PB very well, whereas the $(dM/d\varepsilon_t)$-failure criterion proposed by Bert and Kumar (1980) clearly overestimates the maximum extension strain in bending (see relationship (40) in Part I).

Next, the experimental distributions of the longitudinal (or axial) strain ε_{xx} along the height of a marble beam in four traverses at various distances from the central section are displayed in Figs. 7 and 8 for a small load and for the maximum load at hand, respectively. Since the experimental points coincide with the locations of the strain gages, one can also see in the same graphs, the coordinates of the strain gauge locations. It should be noted here that the four longitudinal strain measurements corresponding to the outermost lower edge of the marble beams were recorded from strain gages attached at mid-depth of the lower surface of the beam.

The above experimental strain diagrams indicate the following:

(1) As far as longitudinal strains are concerned, the central cross-section of the beam is under extension *almost* along its full height. This effect is attributed to the localized effect of the concentrated load or ''punch effect'', which in turn attenuates fast along the height of the beam. According to the numerical calculations presented in the diagram of Fig. 10 of Part I, a compressive deformation zone should also be present directly below the point load; however, due to the fact that this zone is limited in a rather thin skin below the load, it is not possible to be captured by the strain gages.

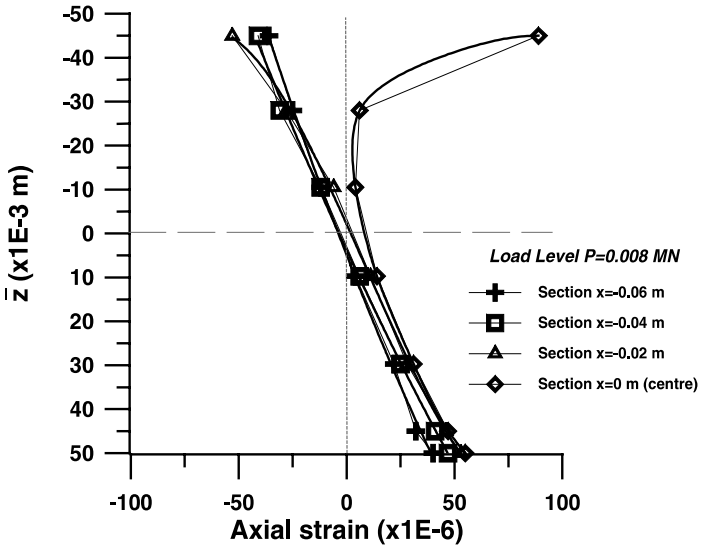

Fig. 7. Experimental distribution of the longitudinal (axial) strain ε_{xx} along the height of the marble beam at load level $P = 0.24P_F$ (test no. IV). The continuous lines represent best-fit polynomials.

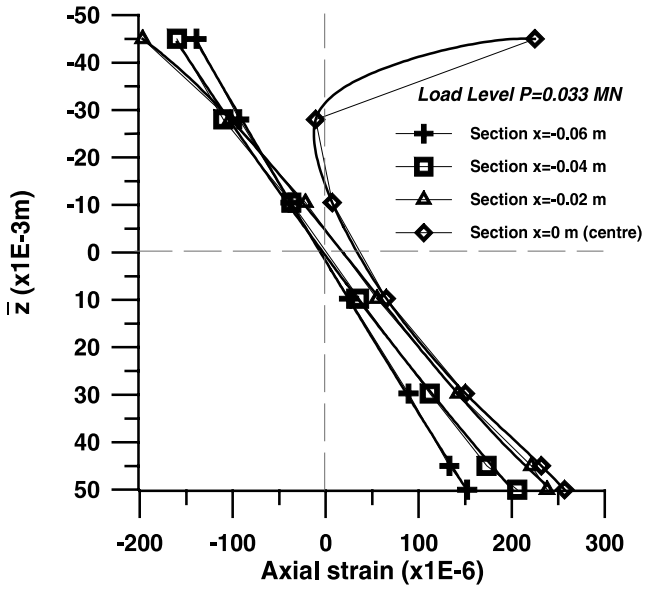

Fig. 8. Experimental distribution of the longitudinal (axial) strain ε_{xx} along the height of the marble beam at load level $P = 0.98P_F$ (test no. IV). The continuous lines represent best-fit polynomials.

(2) At cross-sections away from the central one, the longitudinal strains close to the upper and lower surfaces of the beam deviate from the linear Bernoulli–Euler distribution; thus, plane sections do not remain perfectly plane during loading. This deviation from planarity decreases as one moves away from the central cross-section; thus, the "punch effect" attenuates far from the central section along the longitudinal direction.

(3) The neutral axis of the beam, corresponding to the sections $x = -0.02$, -0.04 and -0.06 m, lies below the middle spanwise axis of the beam (i.e. $\bar{z} = 0$), at small loads, and shifts to this axis as load increases.

Consolidated schematic diagrams of the experimentally measured longitudinal strains across four cross-sections of Dionysos marble beam are presented in Fig. 9(a) and (b) corresponding to two 3PB test nos. III and IV, respectively. From these diagrams, one may note that Saint Venant's principle is satisfied in the present 3PB experiments.

Indeed, from the experimentally measured distributions of longitudinal strains at various cross-sections of the beam (Fig. 9(a) and (b)), it may be seen that near the region of load application, the longitudinal

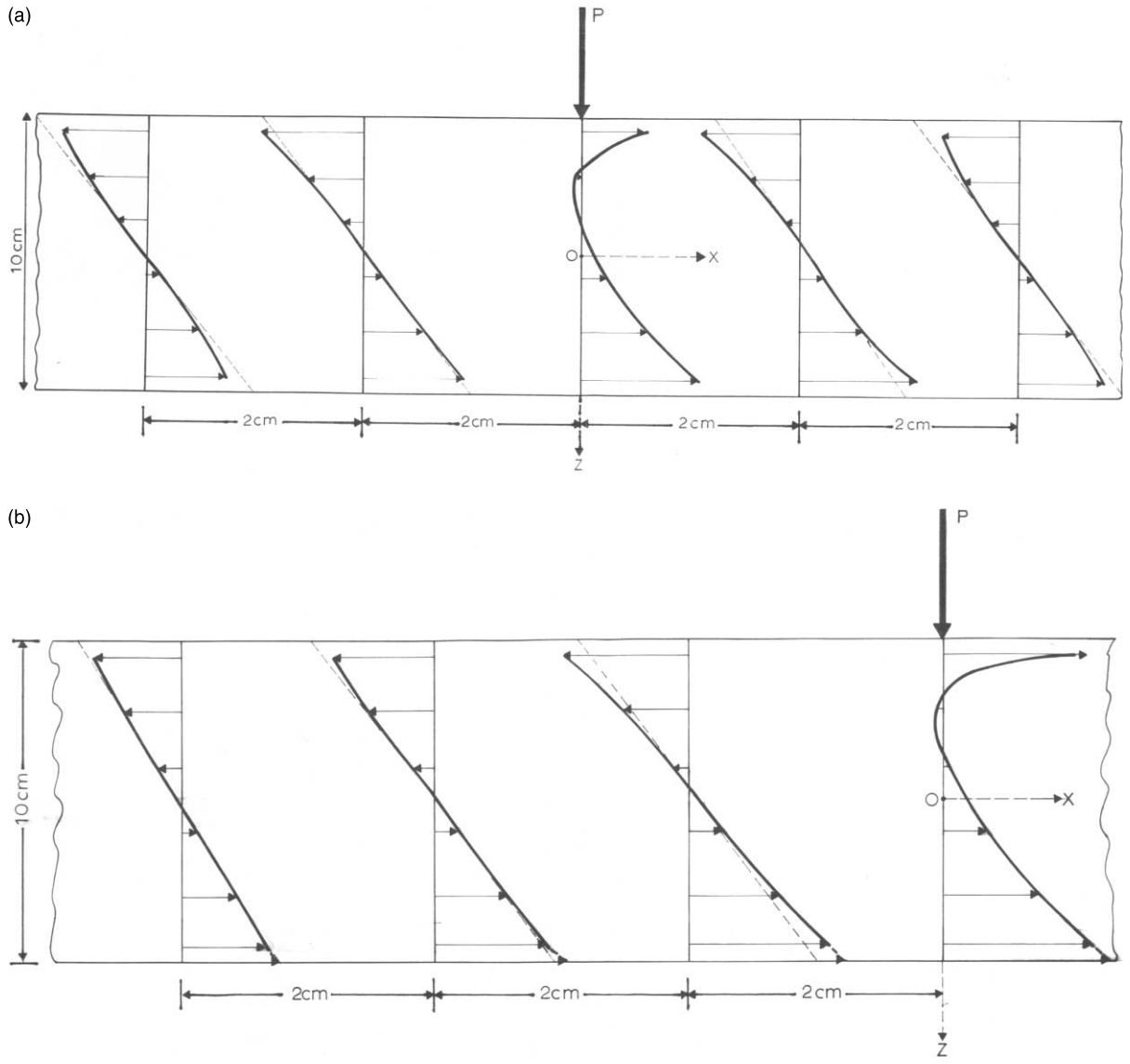

Fig. 9. Schematic diagram of experimentally measured distributions of longitudinal strains ε_{xx} across the beam height at various cross-sections of the Dionysos marble beam at load level 98% of P_F: (a) test no. III and (b) test no. IV.

strain distribution is close to the linear distribution except near the top and bottom surfaces where strains follow a parabolic distribution law. Moreover, as one moves away from the central cross-section, e.g. at $x = -0.06$ m in Fig. 9(b), or at distances from center greater or equal to half the height of the beam ($H/2 = 0.05$ m), longitudinal strains follow the linear distribution. Thus, provided that the measurements we consider are far enough such that this principle is valid, then the assumptions of the nonlinear beam bending theory presented in Part I hold true. As may also be seen in Fig. 9(a), the loading during the 3PB tests is symmetrical about the central axis of the specimen.

Another important experimental observation regarding the 3PB tests on Dionysos marble beams is that the central section is under extension. This observation leads to the conclusion that an extensional mechanism exactly at the central cross-section of the beam is the prominent crack mechanism controlling failure of marble in 3PB test. Furthermore, this finding is in agreement with the results of Part I (e.g. Fig. 10 of Part I), which indicate that for rocks characterized by Poisson's ratio greater than 0.25, the central section is under extensional longitudinal strain. Indeed, as was mentioned above, direct tension tests indicate that $v = 0.26$ for this type of rock. This explains the fact that the critical extension strain in 3PB bending is the same with that in direct tension test and not nearly 1.6 times the respective value in tension as is predicted by the instability criterion $\mathrm{d}M/\mathrm{d}\varepsilon_t = 0$. On the other hand, in 4PB, the central section is under both compressive and tensile longitudinal straining so that the later failure criterion is valid, as it was also shown in the experiments of Laws (1981).

The distributions of longitudinal and transverse strains along the central section of the beam at a sufficiently small load (such that the marble behaves linear elastically) derived from the numerical displacement discontinuity technique (DDT) in plane stress conditions by using formulae (54b) for $m = 0.8$ of Part I, have been plotted in Fig. 10 along with the experimental values from two 3PB experiments. For the computation of longitudinal strains, the values $E_t = 85$ GPa, $v_t = 0.26$ were employed, whereas for the computation of transverse strains, the values $E_c = 71$ GPa, $v_c = 0.31$ were used. From this figure, the very close agreement of numerical and experimental results is illustrated, depicting that the marble behaves as a bilinear elastic material at the load level at hand, and the initial moduli of elasticity $E_t = 85$ GPa and $E_c = 71$ GPa derived from the direct tension and unconfined compression tests, respectively, holds also valid for the whole middle section of the beam.

Next, the last two experimental observations (2) and (3) listed above are investigated with the aid of the numerical model. For this purpose, computed values of the longitudinal strain ε_{xx} along the cross-section $x = -0.06$ m of the beam for the unique-modulus material model (i.e. $m = 1$) in plane stress conditions along with the experimentally measured values are illustrated in Fig. 11.

As is illustrated in Fig. 11, the numerical model predicts the experimentally observed nonlinearity of distribution of longitudinal strains along the height of the beam attributed to the "punch" effect above. Further, it is seen that the numerical model predicts that the neutral axis of the beam at the given section lies exactly at $y = 0$, whereas the experimental evidence indicates that the position of the neutral axis is below the middle section of the beam (i.e. $z_t = 4.8$ cm). Fig. 11 also indicates that (a) the values of the tensile longitudinal strain below the neutral axis predicted by the numerical model agree with the experimental values while a small difference at the outer fiber is attributed to the "plane strain" effect (the strain at the outermost fiber is measured at the mid-depth of the bottom surface of the beam), and (b) the experimental strains begin to deviate from the theoretical distribution at the outermost fiber in tension, and this deviation increases, as the distance from this fiber increases. In fact, from the asymptotic formula (27) of Part I, one may realize that for sufficiently small strains, as the moduli ratio m decreases from the value of one, then the strain ratio $(\varepsilon_c/\varepsilon_t)$ increases from the value of one on and vice versa. From this figure, it may be seen that the experimentally derived strain ratio $(\varepsilon_c/\varepsilon_t)$ is larger than that predicted numerically for $m = 1$, which confirms that the marble under consideration is characterized by $E_c < E_t$. It is worth noting that the same result was derived from the direct tension and unconfined compression tests presented in Section 2. Usually, one has only the value of compressive modulus E_c that is independently measured from a uniaxial

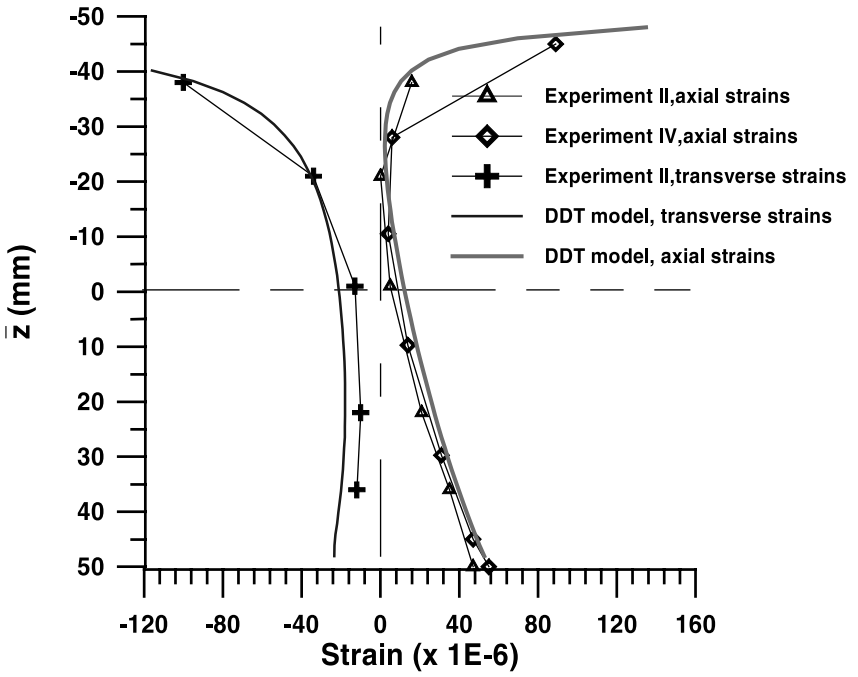

Fig. 10. Comparison of experimental and numerical distributions of longitudinal and transverse strains along the central vertical section of the beam at load level $P = 0.008$ MN (test no. IV).

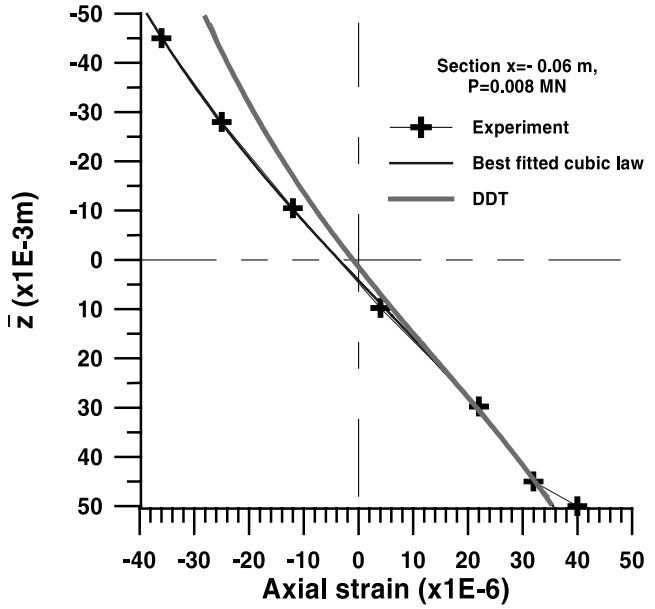

Fig. 11. Comparison of experimental and numerical distributions of longitudinal strain along the vertical section $x = -0.06$ m of the beam for $E = 85$ GPa, $v = 0.26$ and $P = 0.008$ MN (test no. IV).

compression test. It is obvious that if the material is characterized by an elastic modulus in compression lower than in tension, then a unique modulus bending model will predict a higher outermost extension strain than the actual one. In turn, this overestimation of the extension strain will eventually lead to conservative beam design methodologies.

3.2. Back-analysis of experimental bending data

Herein, using the technical bending theory presented in Part I as guidelines, we attempt to back-analyze the experimental data of the bending experiments with the purpose to evaluate the modulus of elasticity ratio m and the damage parameter m_f in the tensile regime of Dionysos marble. Fig. 12 shows a typical plot of the dependence of the position of the neutral axis $\hat{z}_t$ on the magnitude of extension strain deduced from the bending test no. IV on Dionysos marble referring to the section $x = -0.06$ m. This cross-section was chosen, since it lies sufficiently far from the central cross-section of the beam (i.e. more than half the depth of the beam) so that the Saint Venant principle is satisfied and thus, the theory developed in Part I is valid. In the same plot, the best fitted parabolic law with respect to the outer fiber tension strain is also shown, i.e.

$$\hat{z}_t = 0.47 + 57.5\varepsilon_t + 361,498\varepsilon_t^2, \quad 0 \leqslant \varepsilon_t \leqslant 200 \times 10^{-6}. \tag{8}$$

According to the series expansion of the position of the neutral axis of the beam given by relationship (29) in Part I, the value of the zero-order term of this parabola can be used to deduce the modulus ratio m. Indeed, the best fit parabolic curve (8) gives a constant term equal to 0.47

$$\frac{m}{m + \sqrt{m}} = 0.47 \Rightarrow \ m = 0.78. \tag{9}$$

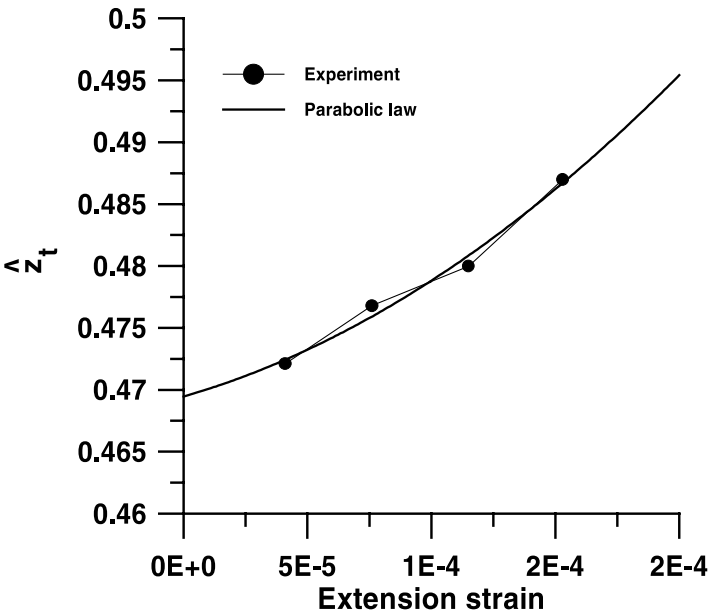

Fig. 12. Graphical representation of the tensile outer-fiber distance $\hat{z}_t$ with tensile strain ε_t referring to bending of Dionysos marble at the section $x = -0.06$ m (test no. IV).

Hence, the present bilinear (or double elasticity) beam theory in conjunction with the experimental bending data agrees very well with the direct tension and uniaxial compression experimental data presented in Section 2.

The dependence of the compressive strain on the tensile strain both measured very close to the upper and lower edges of the beam, at two cross-sections, namely $x = -0.06$ and -0.04 m, respectively, obtained from the bending test no. IV are displayed in Fig. 13(a) and (b). For comparison purposes on the same graphs, the curve $\varepsilon_c = \varepsilon_t$ corresponding to unique modulus, linear elastic material is also illustrated. It turns out that the best fit curve to the experimental data is the parabolic one. By comparing the coefficients of the best fit curve with the coefficients of the series expansion of the compressive strain (27) of Part I, one obtains for the section $x = -0.06$ m

$$\begin{cases} \frac{1}{\sqrt{m}} = 1.12936 \;\Rightarrow\; m = 0.78, \\ \frac{1}{3}\frac{m_f}{\sqrt{m}} = -635.777 \;\Rightarrow\; m_f = -1690, \quad x = -0.06 \text{ m}. \end{cases} \tag{10}$$

On the other hand, at the section closer to the central section of the beam ($x = -0.04$ m), the following relations are valid

$$\begin{cases} \frac{1}{\sqrt{m}} = 1.07 \;\Rightarrow\; m = 0.87, \\ \frac{1}{3}\frac{m_f}{\sqrt{m}} = -726.3 \;\Rightarrow\; m_f = -2036, \quad x = -0.04 \text{ m}. \end{cases} \tag{11}$$

The above results are in very close agreement with the experimental results obtained independently from the uniaxial tension and compression tests (e.g. Section 2). It should be also noticed that the value of the modulus ratio obtained from the strain data at the section $x = -0.06$ m is exactly the same with that obtained from the extrapolation of the position of the neutral axis at zero extension strain, whereas the damage parameter m_f is lower than that found independently from the direct tension tests (i.e. $m_f = -1880$). On the contrary, the strain measurements at the cross-section $x = -0.04$ m indicate larger values for the modulus ratio m and the damage parameter m_f, due to the punch effect.

In Fig. 14, the experimental values of the bending curvature derived from the experimental distribution of the longitudinal strain ε_{xx} along the height of the beam at the load level of $P = 0.98\ P_F$ (Fig. 8), i.e. close to the instant of failure of the beam, are presented. In this figure, the black dot symbols represent the values of the bending curvature by taking the $(d\varepsilon_{xx}/dz)$ derivative of the least squares line at the mid-height of the marble beam. On the other hand, the rhombic symbols correspond to the bending curvature values found as the slopes of the best fit curves at the lower edge of the beam (i.e. at $z = z_t$).

From Fig. 14, it may be seen that moving towards the central region of the beam, the discrepancy of κ values at mid-height and the bottom face increases (at central section, the bending curvature at outermost fiber is approximately twice that taken at neutral axis), whereas it is practically zero at $x = -0.06$ m, i.e. at a distance from the center greater than a half of the height of the beam where Saint Venant's principle is valid. It should be noted that the punch effect appreciably decreases the bending curvature at the central cross-section and at mid-height as compared to that predicted by the bilinear flexure theory ($m = 0.8$) and represented by the continuous thin line in Fig. 14. It is worth noting from the same figure that the prediction of the bilinear bending theory is tangent to the fictitious line passing through the experimental κ values at beam mid-height, whereas it passes through the κ value at bottom fiber located at distance of $x = -0.06$ m from the central cross-section of the beam. On the contrary, κ values at bottom fiber and at distances from the central cross-section that are lower than the half-height of the beam closely follow the prediction of the nonlinear (with damage) bending theory for $m = 0.8$ and $m_f = -1600$. Alternatively, the damage parameter m_f may be found from Eq. (44) presented in Part I by solving for m_f for $m = 0.8$ and expanding into series around the value of m. In this case, it can be found that the following relation is valid

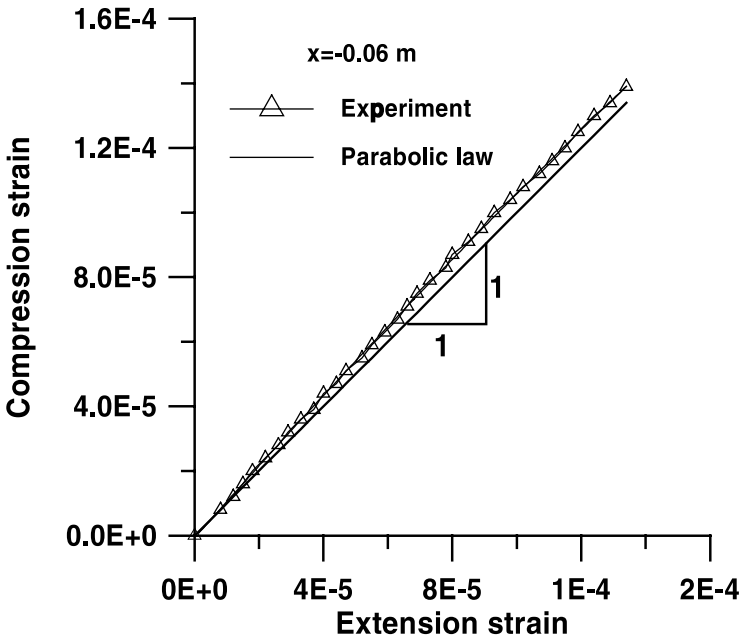

(a)

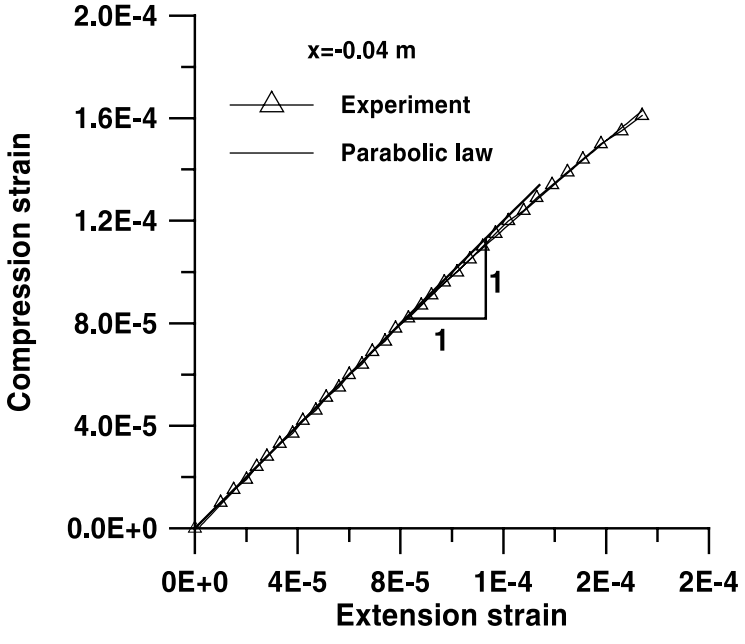

(b)

Fig. 13. Dependence of the outermost compressive strain on the outermost tensile strain at the two normal sections at hand: (a) normal section $x = -0.06$ m, and (b) normal section $x = -0.04$ m.

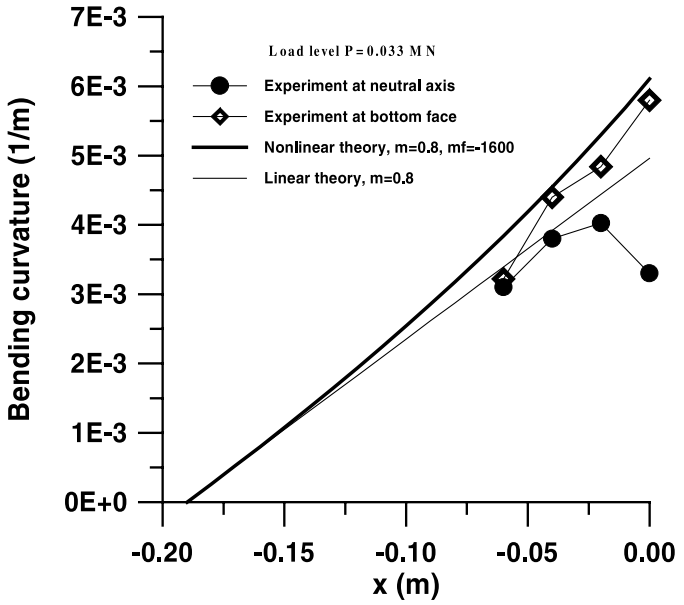

Fig. 14. Bending curvature along the half-length of the beam at 98% of the failure load meausred in the test no. IV. The continuous lines represent the predictions of the nonlinear (thick line) and linear (thin line) bending theories for $E = 85$ GPA, $m_f = -1600$.

$$m_f = -\frac{4}{10\kappa_u}\left[33.9 - 17.8m + 6.7m^2\right] + O[(m-0.8)^3], \tag{12}$$

where κ_u denotes the ultimate bending curvature at the center of the beam. For the value of $\kappa_u = 0.0058\ \mathrm{m}^{-1}$ that have been found from the experiment, formula (12) gives

$$m_f = -1650. \tag{13}$$

The above value of the damage parameter is in full agreement with the respective value found from strain measurements (e.g. second part of Eq. (10)).

Fig. 14 demonstrates that the damage of marble beam in 3PB is developed in that part of the beam that extends between the central cross-section and at a distance approximately one half of beam height at either sides. The central cross-section reaches the highest bending curvature at its outermost fiber earlier than the nearby cross-sections, i.e. failure is localized at the center of the beam and starts from the bottom fiber in contrast to the 4PB test in which fracture can start anywhere between the locations of load application.

Next, load–deflection diagrams of Dionysos marble beam in 3PB at cross-sections $x = -0.04$ m and at center measured during the bending test no. III are presented in Fig. 15. As can be observed from Fig. 15, the deflection measured at $x = -0.04$ m is proportional to the load up to the point of failure. On the other hand, the deflections measured at the central cross-section, namely $x = 0$ m, exhibits nonlinearity with applied central load. The laws which were best fitted to the experimental data presented in Fig. 15 have the following forms:

$$\begin{cases} P = 538w - 64,3000w^2, & x = 0\ \mathrm{m}, \\ P = 653w, & x = -0.04\ \mathrm{m}, \end{cases} \tag{14}$$

wherein w is expressed in m and P in MN.

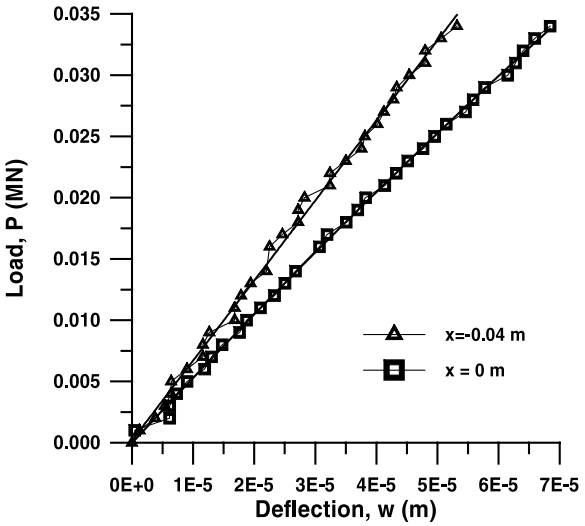

Fig. 15. Experimental load–deflection diagrams in 3PB of Dionysos marble at the sections $x = -0.04$ m and $x = 0$ m (test no. III).

The parabolic law fitted to the load–deflection diagram corresponding to the section $x = 0$ m indicates that this section exhibits microcracking during loading, whereas the section $x = -0.04$ m seems not to accumulate significant damage up to failure load. Even if the load–deflection diagrams presented above were derived from another bending test (test no. III) than that from which the bending curvature diagram was derived (test no. IV) (i.e. Fig. 14), it is shown that both indirect measurements of bending curvature and deflection, respectively, indicate that damage is localized in a region around the central cross-section that is extended approximately one-half of beam height in both sides.

Next, by assuming that the deflection distribution along the axis of the beam is given by the Bernoulli–Euler theory, one may solve with respect to reduced modulus and find

$$\hat{E}_{\mathrm{r}} = \frac{1}{E_{\mathrm{t}} B H^3} x' \left(\frac{3L^2}{4} - x'^2 \right) \frac{P}{w}, \tag{15}$$

where $x' = x + L/2$ we have nondimensionalized E_{r} by dividing it with Young's modulus in tension E_{t}. By computing $\hat{E}_{\mathrm{r}}$ with the aid of formula (15) and load–deflection measurements at $x = -0.04$ m (Fig. 15), taking $E_{\mathrm{t}} = 85,000$ MPa for Dionysos marble, and then plotting it with respect to the outer fiber extension strain occurring at the same cross-section, the plot of Fig. 16 is obtained. From this figure, it may be seen that the normalized reduced modulus remains essentially constant with respect to outermost fiber extension strain; thus, it is in close agreement with the linear load–deflection relation found above and expressed by the second of relation (14). Secondly, it may also be noted from the same figure that the extrapolation of $\hat{E}_{\mathrm{r}}$-data to zero strain gives $\hat{E}_{\mathrm{r}} = 0.90$ that is in close agreement with the prediction of the asymptotic formula (34) of Part I for $m_{\mathrm{f}} = 0$, which for $m = 0.8$ gives $\hat{E}_{\mathrm{r}} = 0.89$. Hence, load–deflection measurements in 3PB and the bilinear bending with no-damage theory at cross-sections far away from the central cross-section – such that Saint Venant's principle is satisfied – can precisely give the elasticity modulus ratio m of the rock at hand.

The dependence of the normalized reduced modulus on outermost extension strain at the central cross-section ($x = 0$ m) is illustrated in Fig. 17. In the same figure, the first-order approximation of $\hat{E}_{\mathrm{r}}$ given by the first two terms of asymptotic expansion (34) of Part I has been also plotted for $m = 0.8$, $m_{\mathrm{f}} = -1600$, that is for Dionysos marble

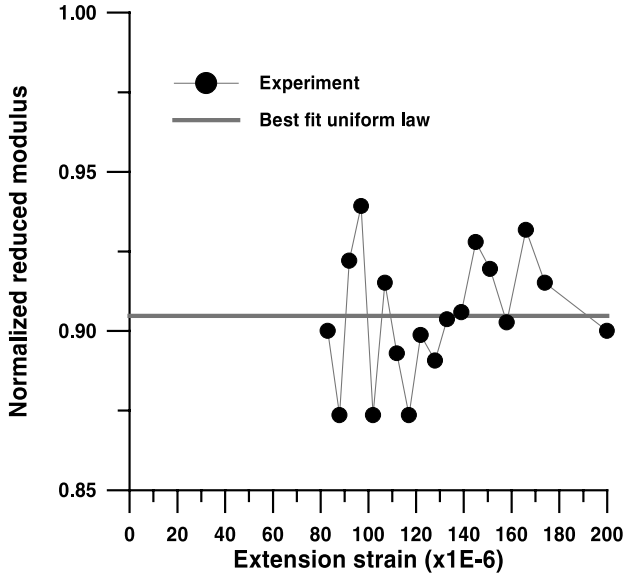

Fig. 16. Plot of normalized reduced modulus $\hat{E}_r$ versus extension strain at lower fiber of Dionysos marble beam at section $x = -0.04$ m (test no. III).

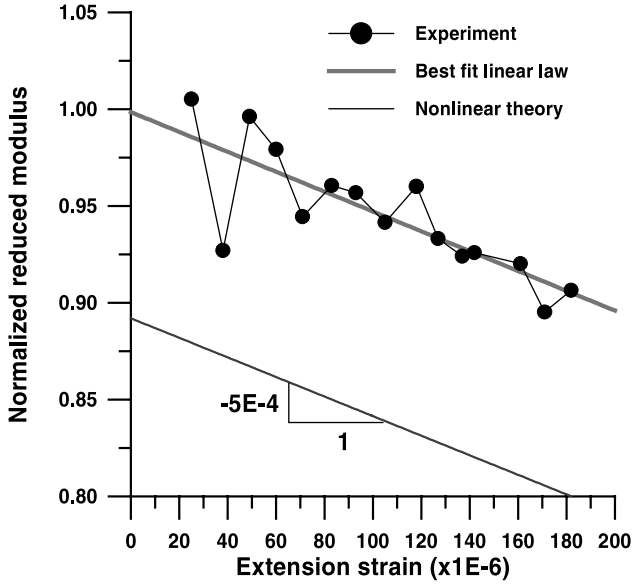

Fig. 17. Plot of normalized reduced modulus $\hat{E}_r$ versus extension strain at lower fiber of Dionysos marble beam at central section $x = 0$ m (test no. III).

$$\hat{E}_r = 0.89 - 505\varepsilon_t + O(\varepsilon_t^2). \tag{16}$$

From Fig. 17, it may be seen that the dependence of reduced modulus with respect to extension strain is linear monotonically descending, which agrees with the first parabolic load–deflection empirical law (14)

corresponding to the same normal section. Further, it is noted that the value of $\hat{E}_r$ at $\varepsilon_t = 0$ is higher than the value of $\hat{E}_r = 0.89$ predicted by the bending theory for $m = 0.8$. However, the slope of the curve, namely $d\hat{E}_r/d\varepsilon_t = -512$ at $x = 0$ m, agrees with the slope of -505 predicted by the nonlinear theory for $m = -0.8$, $m_f = -1600$. The higher value of $\hat{E}_r$ at $\varepsilon_t = 0$ exhibited by the central cross-section may be attributed to the fact that the Bernoulli–Euler theory is not applicable close to central section of the beam due to deviation from planarity of that section, which in turn is caused by the localized load.

The distributions of deflection along the semi-length of the beam that was measured experimentally and predicted by the Bernoulli–Euler and Timoshenko theories, as well as by the nonlinear theory presented herein, are illustrated in Fig. 18. It is recalled herein that the shear-bending Timoshenko's theory predicts the following expression for beam deflection

$$w(x') = \frac{P}{BH^3E_r}x'\left(\frac{3L^2}{4} - x'^2 + 6\ell^2\right) \tag{17}$$

in which the parameter ℓ has the dimensions of length, hence it is a mesostructural length scale that depicts the "shape effect" in Timoshenko's elementary flexure theory. It may be shown that for a linear elastic material, i.e. $E_r = E$, and for a beam of rectangular cross-section, the following relationship is valid

$$\eta^2 = \frac{E(BH^3/12)}{[E/2(1+\nu)](5/6)BHL^2} = \frac{(1+\nu)}{5}\left(\frac{H}{L}\right)^2 \quad \text{or} \quad \eta^2 = \mathrm{O}\left(\left(\frac{H}{L}\right)^2\right), \tag{18}$$

where we have set

$$\eta = \frac{\ell}{L}. \tag{19}$$

From Fig. 18, it may be seen that the prediction of the bilinear theory with no-damage for $m = 0.8$ lies exactly on the deflection measurement at $x = -0.04$ m. This observation is in agreement with the diagram

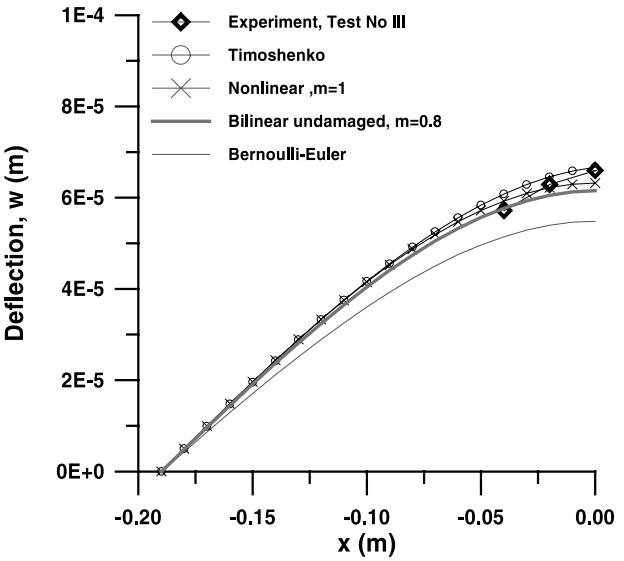

Fig. 18. Experimental (test no. III) and theoretical distribution of marble beam deflection at 98% of the failure load. The theoretical distributions of marble beam deflection predicted by linear Bernoulli–Euler and Timoshenko theories were computed from formulae (15) and (17), respectively, for $E = 85$ GPa, $\nu = 0.3$, $m = 1$, whereas for the nonlinear theory with damage it was taken $m_f = -1600$.

of normalized reduced modulus of Fig. 16. Secondly, the predictions of the nonlinear theory with $m = 1$, $m_f = -1600$ are in accordance with the measurements at the central section of the beam, as already has been demonstrated in the diagram of Fig. 17. The interesting result, however, is that the linear Timoshenko theory (for material that do not exhibits damage) is in very good agreement with measured deflections at the central section and section $x = -0.02$ m of the beam and in turn with the nonlinear theory ($m = 1$, $m_f = -1600$) at the same sections. That is to say, the linear Timoshenko theory reproduces exactly the results of the nonlinear theory at beam central region. The microstructural length scale ℓ may be calculated from Eqs. (18) and (19) above as follows:

$$\ell = 0.051 \text{ m} \quad \Longleftrightarrow \quad \eta = \frac{\ell}{L} = 0.134, \tag{20}$$

Further, by forcing the two theories, namely the nonlinear theory and linear Timoshenko theory, to give the same deflections at the central section of the beam for $m = 0.8$, we obtain the expression

$$\hat{E}_r = \frac{0.89}{1 - 12\eta^2}. \tag{21}$$

It may be observed from this formula that for $\eta = 0$ then $\hat{E}_r \approx 0.9$, whereas for increasing values of η, the reduced modulus increases and reaches the value that has been found independently from deflection measurements at $\eta = 0.134$. Thus, it seems that a linear shear-bending theory containing an intrinsic length scale is able to approximate the nonlinear behavior by an appropriate effective cross-section reduction.

3.3. Bending moment relation, failure load and modulus of rupture of Dionysos marble

Next, the reproducibility of moment versus outermost extension strain at central cross-section of marble beams is demonstrated in Fig. 19. Three of the curves indicated in this figure are referring to monotonic loading, whereas one of them to a cyclic loading.

The dependencies of normalized bending moment on outer-fiber extension strain at central and $x = -0.06$ m sections of the beam found from experiment no. IV and predicted by the nonlinear theory in Eq. (37) of Part I for $m = 0.8$ and $E_t = 85$ GPa are presented in Fig. 20. It is clearly seen from this figure that the nonlinear bending theory appreciably underestimates the slope $d\hat{M}/d\varepsilon_t$ with this effect to be more pronounced for the central section. The proportionality constants of the linear terms in ε_t for the two beam sections are related with that of the nonlinear bending theory as follows:

$$\left.\begin{aligned} &\beta = \tfrac{0.1726}{0.1574} = 1.096, \quad x = 0 \text{ m}, \\ &\beta = \tfrac{0.2154}{0.165} = 1.031, \quad x = -0.06 \text{ m}, \\ &\beta_{DDT} = 1.10, \quad x = 0 \text{ m}, \\ &L/H = 3.8. \end{aligned}\right\} \tag{22}$$

The correction factor β_{DDT} predicted by the DDT model presented in Part I (Eq. (53)) is also displayed in Eq. (22). From these relations, it is illustrated that the correction factors predicted numerically and experimentally for the central beam section are in full agreement. As far as the section $x = -0.06$ m is concerned, it is seen that the principle of Saint-Venant holds true for that section, i.e. the parasitic effect due to concentrated loading is very small for the section that is far from the central approximately half of the beam height (see also Fig. 9(b), which supports this claim).

From Table 1 and formula (56) of Part I, one can compute the following experimental values of the mean and lowest dimensionless failure load λ^*_{min}, λ^*_{mean}, respectively, of the Dionysos marble beams

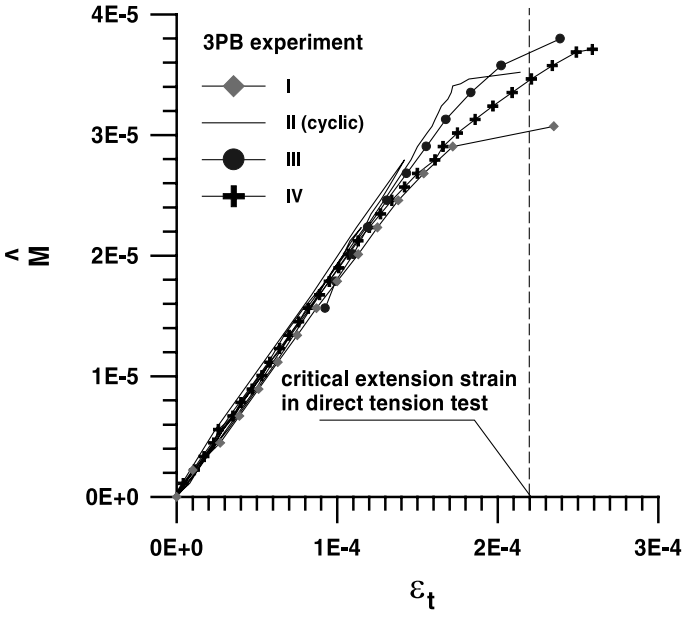

Fig. 19. Reproducibility of normalized moment $\hat{M}$ versus outermost fiber extension strain ε_t relations at central cross-section in the four 3PB experiments on Dionysos marble beams. The value of the critical extension strain at peak load occurred in direct tension tests on marble is represented by the dashed line.

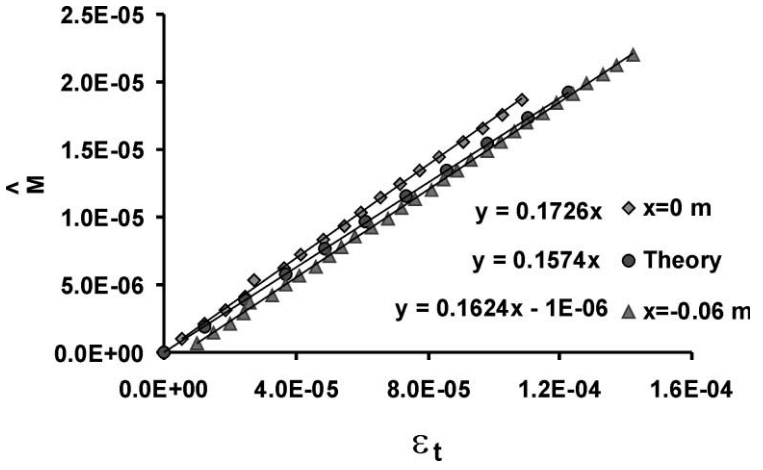

Fig. 20. Experimental and theoretical moment-extension strain diagram in small strains (test no. IV). The theoretical curve was computed from Eq. (48) of Part I for $m = 0.8$.

$$\lambda^*_{\min} = 0.74, \qquad \lambda^*_{\text{mean}} = 0.86. \tag{23}$$

The above experimental values of the dimensionless failure load should be compared to the respective value predicted by the proposed nonlinear theory (e.g. Part I) for $\beta = 1.10$, $m = 8$ and $D_f = 0.5$.

$$\lambda^* = 0.74. \tag{24}$$

From the above comparison of experimental and theoretical λ values, it is inferred that the theory underestimates by approximately 14% the experimental value of the mean experimental value of λ^*, whereas it is identical to the lowest experimental value of λ^*.

From the following formula which gives the modulus of rupture,

$$\sigma_{bu} = \frac{3}{2}\frac{P_F L}{BH^2}, \tag{25}$$

as well as from the minimum and mean values of failure load indicated in Table 1 and the mean value of the tensile strength $\sigma_{tu} = 11$ MPa, one may obtain the following representative values of the experimental tensile strength ratio for Dionysos marble beams, respectively

$$\mu_{min} = 1.43, \qquad \mu_{mean} = 1.64. \tag{26}$$

Further, the theoretical value of the strength ratio predicted by the present nonlinear theory for bending moment correction factor $\beta = 1.10$, elasticity modulus ratio $m = 0.8$ and ultimate damage factor $D_f = 0.5$ may be found to be

$$\mu = 1.48. \tag{27}$$

The comparison of experimental and theoretical μ values presented in Eqs. (26) and (27), respectively, indicates that the theory underestimates the value of the mean experimental value by 10%, whereas it is slightly higher of the minimum experimental value of the strength ratio. In turn, the tensile strength predicted by the value of μ of Eq. (27) and of the experimental mean value of the bending strength of Dionysos marble, i.e. $\sigma_{bu} = 18.05$ MPa, is $\sigma_{tu} = 12.17$ MPa, which is in reasonable agreement with the respective value derived independently by direct tension tests (e.g. Eq. (1)).

4. Uniaxial stress–strain curves from bending test

The stress–strain curves obtained from direct tension or unconfined compression loading are the most common methods used today to evaluate the physical properties of materials. They serve as the starting point in analyses of elastic–plastic or elastic–brittle deformation, and with the rapid progress in numerical methods of solution, there is an increased need for precise σ–ε data. While simple in principle, both uniaxial tension and compression tests are far from trivial and require great care if precise data are to be obtained. An alternative procedure in which tension and compression σ–ε curves could be obtained from a bending test was suggested to the German engineer Herbert by Ludwig Prandtl. Herbert's subsequent analysis and experiments published in 1910 (Herbert, 1910) revealed the fascinating result that both the tension and compression σ–ε curves of a material can be determined with a single bending specimen. The inverse analysis which aims to examine the feasibility of producing accurate σ–ε curves from 3PB tests is based on the formula

$$\sigma_i = \frac{dM(\varepsilon_c + \varepsilon_t) + 2M(d\varepsilon_c + d\varepsilon_t)}{BH^2 d\varepsilon_i}, \quad i = t, c. \tag{28}$$

Next, we turn to the determination of the stress–strain curves of Dionysos marble in tension and compression from longitudinal strain measurements at the outer fibers of the marble beam in bending. For this purpose, the quantities of load P and longitudinal tension and compression strains ε_t, ε_c, respectively, measured at each cross-section are stored in arrays in such a way that values of the same index correspond to the same time during the test. Therefore, the values used in Eq. (28) all have the same index. The differentials were calculated using the four-point differentiation formula

$$\mathrm{d}f(n) = \tfrac{1}{12}[f(n-2) + 8f(n-1) - 8f(n+1) - f(n+2)], \tag{29}$$

where $f(n)$ refers to the nth data point.

The uniaxial tension stress–strain curve obtained from the bending test at cross-section $x = -0.06$ m is shown in Fig. 21. This normal section of the beam was chosen based on the above observations, which show that it is distant enough from the central section such that the Saint Venant's criterion is satisfied. In this diagram, the points represent the results from a bending test whereas the solid lines represent the following best fit parabolic laws

$$\begin{aligned} &\sigma_t = 84,000\varepsilon_t(1 - 1550\varepsilon_t), \\ &\sigma_c = 66,000\varepsilon_c, \qquad x = -0.06 \text{ m}. \end{aligned} \tag{30}$$

The ratio of initial moduli of elasticity and damage parameter have the values

$$m = \frac{66,000}{84,000} = 0.79, \qquad m_f = -1550. \tag{31}$$

The above values agree with the direct tension and uniaxial compression experimental results illustrated in Section 2, as well as with the other indirect bending measurements presented in Section 3. The results obtained from the other bending experiments in the series showed no significant differences. Relationships (30) and (31) indicate striking agreement with the predictions of the conventional direct tension and unconfined tests.

Further, in Fig. 22, the uniaxial tension and compression versus axial strain curves derived from 3PB data at cross-section $x = -0.04$ m that is closer to the central section of the beam are displayed. The quantitative forms of these curves are given by the relationships

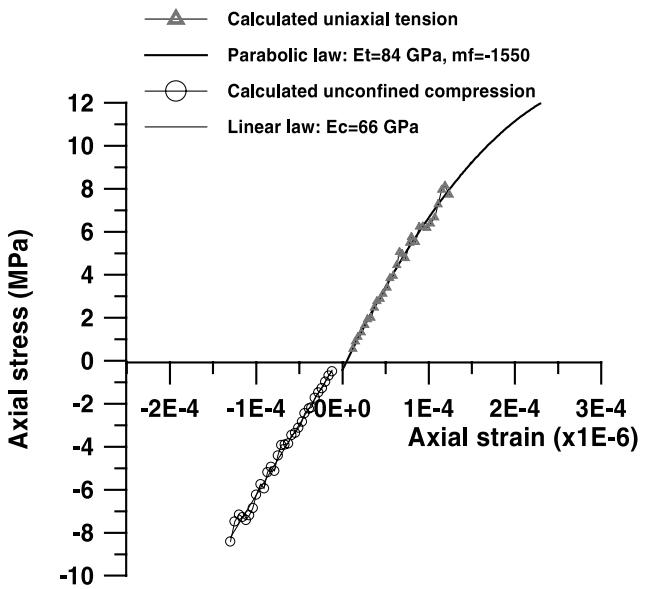

Fig. 21. Derivation of axial stress versus axial strain curves in uniaxial tension and compression from 3PB test no. IV data and formula (28) corresponding to the cross-section $x = -0.06$ m.

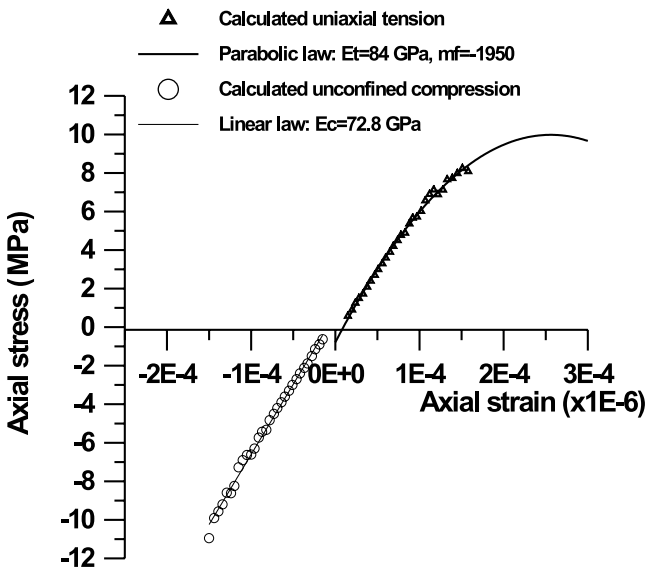

Fig. 22. Derivation of axial stress versus axial strain curves in uniaxial tension and compression from 3PB test no. IV data and formula (27) corresponding to the cross-section $x = -0.04$ m.

$$\begin{aligned} &\sigma_t = 84,000\varepsilon_t(1 - 1950\varepsilon_t), \\ &\sigma_c = 72,800\varepsilon_c, \qquad x = -0.04 \text{ m}. \end{aligned} \tag{32}$$

From the above relationships (32), it can be inferred that

$$m = \frac{72,800}{84,000} = 0.87, \qquad m_f = -1950. \tag{33}$$

It may be observed that the above results for the modulus ratio m and damage parameter m_f referring to the two cross-sections are also in agreement with the results derived independently from the analysis of the outer-fiber extensional and compressive strains in Section 3.2.

Finally, Poisson's ratio of Dionysos marble can be obtained from transverse and axial gauges attached at the bottom surface of the beams. Fig. 23 displays the experimental diagram of transverse strain (ε_{yy}) versus longitudinal strain (ε_{xx}) and the best fit cubic curve that has the form

$$\varepsilon_{yy} = -0.3173\varepsilon_{xx} - 0.0011\varepsilon_{xx}^2 + 8 \times 10^{-6}\varepsilon_{xx}^3, \tag{34}$$

where ε_{xx}, ε_{yy} are expressed in strains. The initial value of the tangent Poisson's ratio of Dionysos marble may be obtained directly from the above equation as follows

$$v = -\frac{\partial\varepsilon_{yy}}{\partial\varepsilon_{xx}} = 0.3173 + \mathrm{O}(\varepsilon_{xx}). \tag{35}$$

The above value of initial Poisson's ratio is in full agreement with the average value of 0.32 measured in the series of uniaxial compression tests, whereas it is somewhat higher than the value of 0.26 measured from the direct tension tests. This result may be attributed to the orthotropic anisotropy displayed by this type of marble.

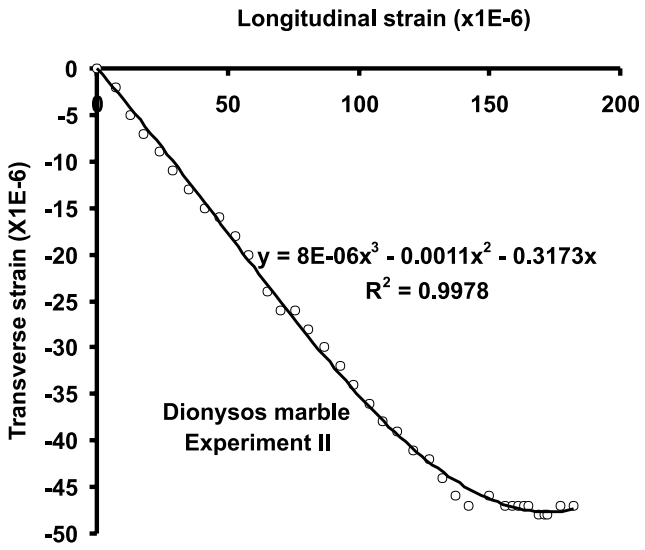

Fig. 23. Plot of transverse strain versus longitudinal strain at bottom surface of the beam (test no. II). Poisson's ratio of Dionysos marble in the linear elastic regime is found from the best fit polynomial curve to be $\nu = 0.3173$.

5. Conclusions

The conclusions of the technical bending theory introduced in Part I have been employed herein as guidelines for the characterization of the mechanical properties of Dionysos marble. It was demonstrated that in order to overcome the difficulties that are inherent to direct tension testing of quasi-brittle rocks and rock-like materials (i.e. concrete, ceramics, etc.), a simpler 3PB test can be performed on rectangular prismatic specimens. Provided that the results of flexure testing of rock beams are properly analyzed, the required moduli of elasticity and the damage parameter in uniaxial tension, as well as the initial modulus of elasticity and "stiffening" parameter in uniaxial compression, may be determined. It should be mentioned that the damage factor of rocks in uniaxial compression cannot be determined from a bending test due to the following two facts: (i) quasi-brittle rocks and rock-like materials such as ceramics and concrete are characterized by a much higher failure compressive strain, i.e. one order of magnitude, than failure extensional strain, and (ii) rock beams fail always in extension; thus, a rock beam fails always prior to the manifestation of damage due to cracking at the compressive region of the beam. Therefore, flexure tests on rocks should always be combined with unconfined compression tests in order to fully characterize the rock in the tension–compression regime.

The present experimental study regarding the 3PB tests on Dionysos marble beams has shown that the proposed technical theory of Part I is valid at sufficiently large distances from the central section of the beam (approximately one half of the beam height) such that Saint-Venant's principle is satisfied. By comparing the bending results (both from strain-gauge measurements and deflections) with those obtained independently from unconfined compression and uniaxial tension tests on rock specimens cored from the same block, a very good agreement was obtained regarding the elasticity and damage material properties in the uniaxial tensile regime and the elasticity of the marble in the compressive regime.

3PB tests and independently conducted uniaxial tension and compression tests indicate that Dionysos marble exhibits a larger initial modulus of elasticity under tensile loading in comparison to the compressive loading. More specifically, it was found that $E_c/E_t \cong 0.8$ with this characteristic behavior of this type of rock shown in Fig. 5. A plausible physical explanation for this special type of anisotropy that is also ex-

hibited by many composite materials (Jones, 1977) has yet to be made. Investigation of the micromechanical behavioral aspects of rock-like materials may lead to a rational explanation of this phenomenon. This observed difference may be attributed either to

- pure micromechanical reasons, such as the complex microstructure of this type of metamorphic rock associated with a complex previous loading history (metamorphism), or
- phenomenological reasons, for example linear curve-fitting of the σ–ε compression curve in small loads.

However, it should be noted here that this relatively small observed anisotropy of Dionysos marble may be associated with certain regions inside the quarry.

Another important experimental observation of this work was that the central section of marble beams is under extension. This phenomenon is attributed to the combination of punch and Poisson's effects and is responsible for the same approximately failure extensional strain in 3PB and direct tension tests. It was also illustrated that a linear shear-bending theory containing an intrinsic length scale, such as Timoshenko's beam theory, is able to approximate the nonlinear deflection behavior of Dionysos marble beams. Further, it was experimentally demonstrated for the beam geometry at hand ($L/H = 3.8$) that the proposed in Part I correction formula for the bending stresses at the bottom fiber of the beam in 3PB at its midsection is valid. This correction has been applied afterwards for the derivation of the failure load and modulus of rupture over tensile strength ratio of Dionysos marble.

Acknowledgements

The authors gratefully acknowledge the financial support of the European Union DG XII, SMT Programme under the contract SMT4-CT96-2130. Further, the authors acknowledge the remarks that have made by the anonymous reviewers.

References

Bert, C.W., Kumar, M., 1980. Discussion of Ref. (Krajcinovic, D. (1979). Distributed damage theory of beams in pure bending. J. Appl. Mech., 46, 592–596). J. Appl. Mech. 47, 449–450.

Exadaktylos, G.E., Vardoulakis, I., Kourkoulis, S.K., 2000. Influence of nonlinearity and double elasticity on flexure of rock beams-I Technical theory. Int. J. Solids Struct., submitted for publication.

Griffith, A.A., 1924. Theory of rupture. Proc. First Int. Congr. Appl. Mech., Delft, pp. 55–63.

Herbert, H., 1910. Uber den Zusammenhang der Biegungselastizitat des Gusseisens mit seiner Zug and Druckelastizitat (On the connection between deformation and tension and compression deformation for cast iron). Mitt. Und Forschungsarb, Ver, deut Ing. 89, 39–81.

Jones, R.M., 1977. Stress–strain relations for materials with different moduli in tension and compression. AIAA J 15 (1), 16–23.

Korres M, 1993. From Pendeli to Parthenon. Melissa, Athens, Greece.

Laws, V., 1981. Derivation of the tensile stress–strain curve from bending data. J. Mater. Sci. 16, 1299–1304.

Stacey, T.R., 1981. A simple extension strain criterion for fracture of brittle rock. Int. J. Rock Mech. Min. Sci. Geomech. Abstr. 18, 469–474.

Vardoulakis, I., Kourkoulis, S.K., Pazis, D., Andrianopoulos, N.P., 1995. Mechanical behavior of Dionysos marble in direct tension. Proc. Felsmechanik Kolloquium, Karlsruhe, Germany.

Vardoulakis, I., Stavropoulou, M., Papadopoulos, C., 1998. Direct tensile properties of Dionysos marble. SMT Report, NTUA.

Zambas, C., 1994. Mechanical properties of Pentelic marbles. Committee for the restoration of Parthenon publications, Athens.